ADVANCED FUNCTIONAL MATERIALS
www.afm-journal.de

Toward Stable p-Type Thiophene-Based Organic Electrochemical Transistors

*Silan Zhang, Penghui Ding, Tero-Petri Ruoko, Ruiheng Wu, Marc-Antoine Stoeckel, Matteo Massetti, Tiefeng Liu, Mikhail Vagin, Dilara Meli, Renee Kroon, Jonathan Rivnay, and Simone Fabiano**

Operational stability is essential for the success of organic electrochemical transistors (OECTs) in bioelectronics. The oxygen reduction reaction (ORR) is a common electrochemical side reaction that can compromise the stability of OECTs, but the relationship between ORR and materials degradation is poorly understood. In this study, the impact of ORR on the stability and degradation mechanisms of thiophene-based OECTs is investigated. The findings show that an increase in pH during ORR leads to the degradation of the polymer backbone. By using a protective polymer glue layer between the semiconductor channel and the aqueous electrolyte, ORR is effectively suppressed and the stability of the OECTs is significantly improved, resulting in current retention of nearly 90% for ≈2 h cycling in the saturation regime.

1. Introduction

Organic mixed ionic–electronic conductors (OMIECs) leverage efficient ion-electron transport capabilities for a range of applications in energy storage[1] and conversion,[2] electrocatalysis,[3] electrochromic display technologies,[4] and bioelectronics.[5] As the channel material in organic electrochemical transistors (OECTs), OMIECs have enabled a variety of exciting applications, including bio-/chemical-sensing,[6] medical diagnostics,[7] and low-voltage/neuromorphic electronics.[8] This rapid development has been driven by advances in materials synthesis[8h,9] and device design/fabrication,[5d,8g,10] as well as an in-depth understanding of the role of polymer microstructure on charge/mass transport mechanisms[11] enabling high charge carrier mobilities and fast device temporal responses.[11a,f,12]

One common strategy to promote electric charge/ion transport in OMIECs is functionalizing their polymer backbones with hydrophilic/polar side chains, such as the case of the p-type (hole-transporting) bithiophene–thienothiophene copolymer bearing tetraethylene glycol side chains (P($g_4$2T-TT), see chemical structure in **Figure 1**a).[13] However, the much-improved materials' ionic conductivity comes

S. Zhang, P. Ding, M.-A. Stoeckel, M. Massetti, T. Liu, M. Vagin, R. Kroon, S. Fabiano
Laboratory of Organic Electronics
Department of Science and Technology
Linköping University
Norrköping SE-601 74, Sweden
E-mail: simone.fabiano@liu.se

S. Zhang, R. Kroon, S. Fabiano
Wallenberg Wood Science Center
Linköping University
Norrköping SE-601 74, Sweden

T.-P. Ruoko
Smart Photonic Materials
Faculty of Engineering and Natural Sciences
Tampere University
Tampere 33720, Finland

R. Wu
Department of Chemistry
Northwestern University
Evanston, IL 60208, USA

D. Meli
Department of Materials Science and Engineering
Northwestern University
Evanston, IL 60208, USA

J. Rivnay
Department of Biomedical Engineering
Northwestern University
Evanston, IL 60208, USA

J. Rivnay
Simpson Querrey Institute
Northwestern University
Chicago, IL 60611, USA

The ORCID identification number(s) for the author(s) of this article can be found under https://doi.org/10.1002/adfm.202302249

DOI: 10.1002/adfm.202302249

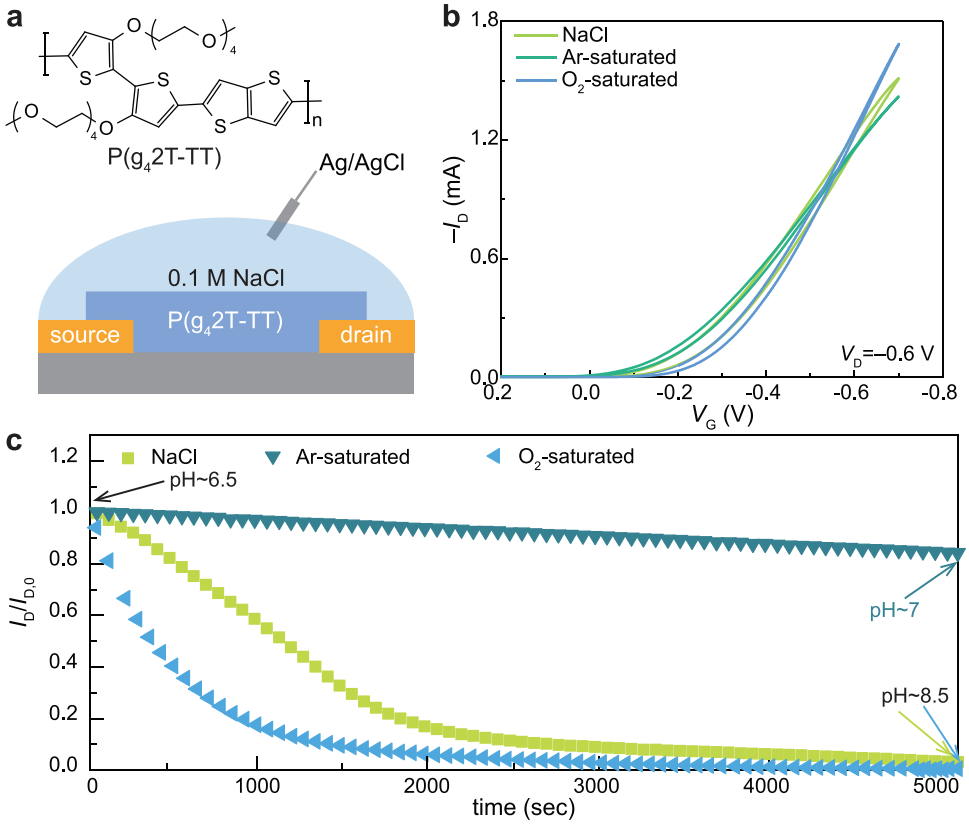

Figure 1. a) Schematic of OECT structure and chemical structure of P($g_4$2T-TT). b) Transfer characteristics of P($g_4$2T-TT)-based OECTs in 0.1 M pristine, Ar-saturated, and O_2-saturated NaCl, respectively (W = 1000 µm, L = 30 µm). c) Corresponding operation stability measurements by pulsing the gate voltage between V_G = 0.15 V to V_G = −0.6 V at constant V_D = −0.6 V. The data are extracted from the on current for each cycle and normalized with the first on current (7 skip points).

at the expense of the devices' operational stability, primarily due to swelling of the channel material[11f,14] and/or electrochemical side reactions such as the oxygen reduction reaction (ORR).[9d] While the former can be suppressed by, e.g., side chain redistribution,[14] adding alkyl spacers to the side chain,[15] or decreasing the length of the side chain,[16] the latter stems from the low ionization energy (IE) of OMIECs carrying glycolated side chains, which make them susceptible to react with oxygen in the electrolyte and lead to fast degradation upon electrochemical doping/dedoping cycles.[17] Although p-type OMIECs are typically more stable than n-type (electron-transporting) OMIECs,[18] their device operational stability is still unsatisfactory for many (bio-)electronic applications. Therefore, both material and device engineering strategies are required to address this issue.

Degassing the electrolyte is the most facile way of suppressing ORR.[11g,17] Yet, working with O_2-free electrolytes is impractical when developing bioelectronic devices that must sense the external environment. At pH 7 in an aqueous environment, the ORR can occur via either a two-electron ($O_2 + 2H^+ + 2e^- \rightarrow 2H_2O_2$, ≈0.28 V versus normal hydrogen electrode) or a four-electron ($O_2 + 4H^+ + 4e^- \rightarrow 2H_2O$, ≈0.81 V vs normal hydrogen electrode) process.[19] This suggests that OMIECs with high IE (i.e., >|4.8| eV), such as diketopyrrolopyrrole (DPP)-based polymers,[9d,20] could hinder the formation of H_2O_2 (two-electron ORR), thereby enhancing device stability as compared to OMIECs with low IE.[9d] However, DPP-based polymers still undergo four-electron ORR and exhibit significant degradation when cycled over an extended period.[9d] In addition, an IE > |4.8| eV translates into a large oxidation potential, which causes the OECTs' threshold voltage (V_{th}) to increase to values typically larger than |0.4| V.[20b] This pushes the device to operate near the electrochemical stability window of the aqueous electrolyte, leading to polymer backbone degradation by side chain cleavage[9d] and high power consumption.[21] While the use of Lewis acids can suppress ORR to some extent,[22] it still results in a halving of the drain current after 80 min of cycling. Therefore, it is important to understand the mechanisms of material degradation during ORR and find ways to prevent it without negatively impacting other device metrics to create stable and safe bioelectronic devices.

Here, we unravel the degradation mechanism of the benchmark polymer P($g_4$2T-TT) during electrochemical doping/dedoping in OECTs and report a simple strategy to prevent faradaic ORR side reactions from occurring during device operation. By using a combination of cyclic voltammetry, ex–situ Raman and infrared spectroscopies, and X-ray scattering measurements, we show that ORR occurs near the drain electrode with hydroxide (OH^-) formation. OH^- is a by-product of ORR, regardless of whether the process involves two or four electrons, and can react with the oxidized polymer backbone causing

irreversible chemical degradation. The latter can be prevented by using a polymer gel composed of polyethylene oxide (PEO) and lithium bis(trifluoromethanesulfonyl)imide (LiTFSI). When the PEO:LiTFSI polymer gel is placed on top of P($g_4$2T-TT), it suppresses water and oxygen permeability and avoids the formation of reactive ORR by-products, thus yielding OECTs with stable device performance.

2. Results and Discussion

To understand how the electrolyte's O_2 content affects the device stability, we investigated the OECT performance using 1) pristine, 2) Ar-saturated, and 3) O_2-saturated 0.1 M NaCl aqueous electrolytes. The typical P($g_4$2T-TT)-based OECT transfer characteristics, measured at $V_D = -0.6$ V for the three electrolytes, are reported in Figure 1b and Figure S1 (Supporting Information) and show negligible variations in saturated drain current independent of the electrolyte's O_2 content.

We then measured the device's stability in the different electrolytes by continuously pulsing V_G from 0.15 V to −0.6 V (pulse width = 5 s) for more than 500 cycles (Figure S2, Supporting Information). Figure 1c shows the evolution of I_D normalized to the initial I_D values ($I_{D,0}$) for $V_G = -0.6$ V. P($g_4$2T-TT)-based OECTs measured in pristine NaCl retain only 3% of the initial drain current at the end of the 510 cycles, with I_D dropping by more than 80% after 30 min of continuous operation. This effect is even more pronounced when the OECTs are measured using an O_2-saturated NaCl electrolyte, with only 10% of the initial I_D retained after 15 min. In stark contrast, OECTs measured using an Ar-saturated NaCl electrolyte retained 84% of the initial I_D at the end of the 510 cycles. Interestingly, we noticed that the electrolytes' pH changed during the cycling test, going from 6.5 (initial) to 8.5 (final) for pristine and O_2-saturated NaCl electrolytes and from 6.5 (initial) to 7.0 (final) for Ar-saturated NaCl electrolyte.

To investigate whether the increase in pH is responsible for the device's current degradation, we measured the P($g_4$2T-TT)-based OECTs in NaCl by adjusting its pH to 8 with small amounts of 0.1 M NaOH and observed faster degradation compared to pristine NaCl, with only 1% of I_D after ≈510 cycles (Figure S3. Supporting Information) with a final pH of ≈9.5. Using 100 mM phosphate-buffered saline (PBS) solution improves the device's stability, with 94% of the initial I_D retained after 85 min (Figure S4, Supporting Information). However, at 10 mM PBS buffer concentration, only 16% of initial I_D is retained after 85 min of continuous operation, suggesting that low buffer concentrations could counteract the formation of excessive OH^- only up to ≈300 cycles but fails for long-term operation (Figure S4, Supporting Information).

We hypothesize that OH^- is one of the by-products of ORR occurring in the aqueous electrolyte during the OECT operation. P($g_4$2T-TT) has an ionization potential of ≈4.4 eV,[23] and is known to promote ORR.[9d] As the Ag/AgCl gate electrode is a nonpolarizable material, its standard electrode potential does not change significantly when current is passed through it. Figure S5 (Supporting Information) shows the Ag/AgCl paste voltage calibration in 0.1 M NaCl solution (vs standard Ag/AgCl electrode with saturated KCl as the supporting electrolyte) at 0.5 and 5 μA constant currents (same current range as the gate current during OECT operation). The potential difference between the Ag/AgCl paste and standard Ag/AgCl is ≈0.1 V. As the OECTs are operated by tuning V_G from 0.2 to −0.7 V with a constant $V_D = -0.6$ V with respect to the source electrode, we calibrated the electrode's potential range of the source and drain electrodes as shown in **Figure 2**a. For a device switching from off to on, the source and drain electrodes work in the electrode's potential range of −0.1 to 0.8 V and −0.7 to 0.2 V, respectively. Note that the calibration of the electrode's potential agrees well with recent reports using different biasing schemes.[17] As ORR in conducting polymers is likely to occur at a negative potential (vs Ag/AgCl standard electrode) for pH 7,[3a,24] we suggest that ORR occurs at the drain electrode when the device is in the off state and that the excess OH^- diffuses from the drain to the source region causing irreversible degradation of P($g_4$2T-TT) while the OECT gradually turns on.

The ORR activity of P($g_4$2T-TT) was evaluated via linear sweep voltammetry (LSV) using a rotating disk electrode (RDE) with voltage swept from 0.2 to −0.8 V versus standard Ag/AgCl. Figure 2b shows the LSV curves obtained under different rotating speeds. The O_2 reduction current increases with increasing the rotating speed, as expected from the Koutecký–Levich equation[25] (see details in the Experimental Section). From the Koutecký–Levich plot reported in Figure S6 (Supporting Information), we then extracted a value of $n = 2$ for different potentials (Figure 2c), suggesting that ORR in P($g_4$2T-TT) follows a 2-electron path with the formation of H_2O_2. The latter was also detected in the OECT's electrolyte after cycling the device for 3 h, using a horseradish peroxidase-3,3′,5,5′-tetramethylbenzidine assay (see the Experimental Section for more details). H_2O_2 interacts with 3,3′,5,5′-tetramethylbenzidine with the help of the horseradish peroxidase, changing the solution from colorless to blue. The concentration of H_2O_2 is then calculated from the absorption peak intensity at 652 nm (Figure S7, Supporting Information).[26] As shown in Figure 2d, the final H_2O_2 concentration after OECT cycling in the pristine and O_2-saturated NaCl solutions is ≈73 and ≈89 μM, respectively. We also detected ≈15 μM of H_2O_2 in the Ar-saturated NaCl solution, possibly due to the system not being completely airtight. Thus, the OH^- formation results from ORR as outlined in the reaction scheme of Figure 2c. Figure 2e shows the OECT's transfer characteristics recorded in 0.1 M degassed NaOH solution as an extreme example of a highly alkaline condition. The transfer curves show large hysteresis, low current level, and complete degradation after only five cycles, suggesting that OH^- contributes greatly to the device degradation. To investigate the possibility that superoxide serves as an intermediate in the ORR process, leading to the formation of OH^-, we added tetrazolium blue chloride (BTC) to the electrolyte to detect the presence of superoxide (Figure S8, Supporting Information). Superoxide reacts with BTC to produce a blue diformazan pigment.[27] However, the electrolyte's UV–vis spectra show no significant changes before and after cycling for 4 h (Figure S8b, Supporting Information), indicating that the ORR pathway of P($g_4$2T-TT) does not involve the formation of superoxide.

To investigate the impact of H_2O_2 on the stability of OECTs, a trace amount of MnO_2 (<0.1 mg in 45 μL electrolyte) was added to the pristine NaCl electrolyte as a catalyst to decompose the generated H_2O_2.[28] After 85 min of cycling, the device retained only 12% of its initial I_D (Figure S9a, Supporting Information).

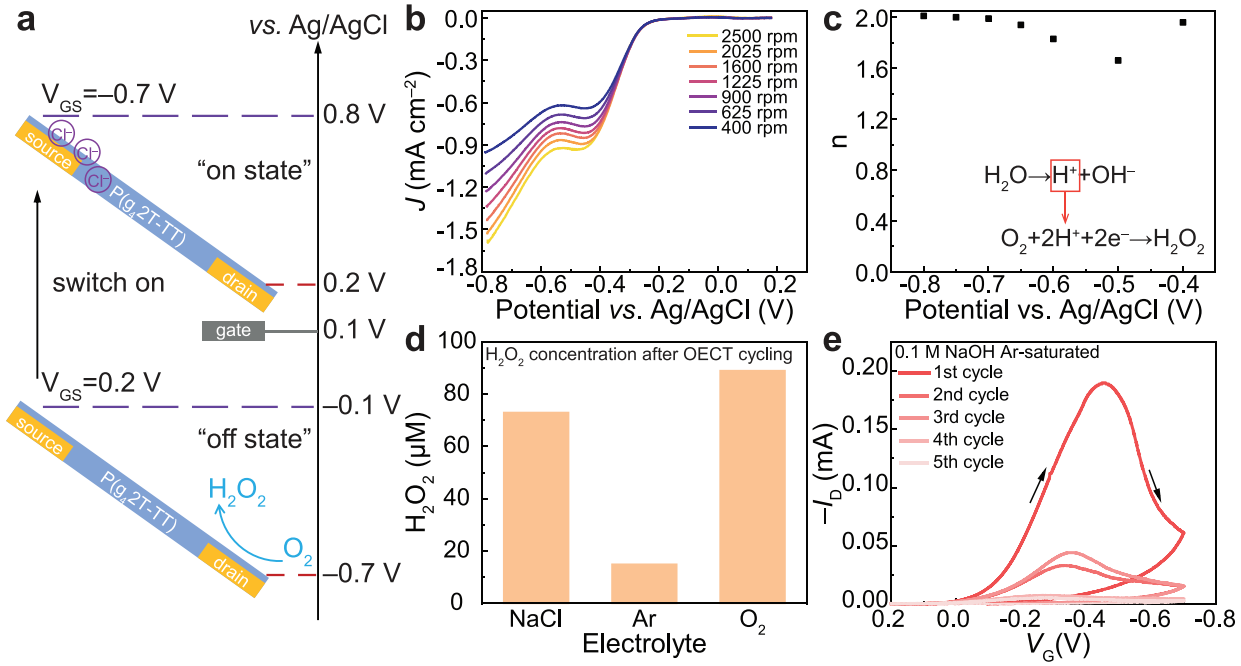

Figure 2. a) Electrode potential calibration of gate, source, and drain electrodes during the OECT operation. b) Linear sweep voltammograms of a P($g_4$2T-TT) film in the O_2-saturated electrolyte under different rotation speeds. c) Electron transfer number obtained from the Koutecký–Levich plot. d) The H_2O_2 concentration in OECT electrolyte after cycling in pristine, Ar-saturated and O_2-saturated 0.1 M NaCl. e) Transfer characteristics of P($g_4$2T-TT)-based OECTs in 0.1 M Ar-saturated NaOH.

Additionally, we measured 19 μM of H_2O_2 in the electrolyte after 3 h of cycling (Figure S9b, Supporting Information). This concentration is comparable to the amount present in P($g_4$2T-TT)-based OECTs in Ar-saturated electrolyte, suggesting that H_2O_2 does not significantly contribute to the OECT's degradation.

We then measured Raman microspectroscopy from the channel, drain, and source regions of P($g_4$2T-TT) OECTs after cycling in NaCl electrolytes with different O_2 content (**Figure 3**a,b and Figure S10, Supporting Information). The Raman spectra of pristine P($g_4$2T-TT) C=C vibrations of thiophene and thienothiophene rings are in the 1300–1550 cm^{-1} range (see Table S1, Supporting Information, for peak assignments). Changes in the Raman spectra after OECT cycling are localized to the source electrode and visible only after cycling in pristine and O_2-saturated NaCl. Both symmetric (1450 cm^{-1}) and antisymmetric (1498 cm^{-1}) thiophene C=C vibrations[29] weaken after cycling with a new strong peak growing at 1516 cm^{-1}. We assign this peak to an antisymmetric thiophene C=C vibration in disordered P($g_4$2T-TT). Similar disorderinduced spectral changes of the thiophene C=C vibration have been observed due to chain twisting,[30] intercalation,[29c] and swelling in electrolytes.[29a] However, the changes we observe cannot be simply due to disorder induced by ion intercalation or swelling of the polymer films since all OECTs were cycled in the same electrolyte but with different O_2 content. This means that the observed Raman changes after cycling are presumably due to structural disorder induced by a chemical reaction in P($g_4$2T-TT).

The Raman spectra of the samples cycled using cyclic voltammetry (CV) scans (Figure S11, Supporting Information) revealed significant changes only in the O_2-saturated electrolyte, while changes in the pristine NaCl electrolyte were minimal. This is likely due to the low concentration of OH^- in a large amount of electrolyte. The sample cycled in NaOH using CV scans between −0.2 and 0.7 V (outside the ORR potential range) versus Ag/AgCl showed the same changes as those observed at the source electrodes of the OECTs (Figure S12, Supporting Information). This demonstrates that OH^- plays a significant role in the degradation process.

The samples that were cycled using CV were also analyzed using Fourier-transform infrared spectroscopy (FTIR) to gain a deeper understanding of the chemical structure changes (Figure 3c). The C–H out-of-plane bending vibration of thiophene at 800 cm^{-1} gradually decreases as the O_2 content increases and is almost completely absent, only visible as a minor shoulder in O_2-saturated NaCl. The appearance of O–H bending (1260 cm^{-1}, phenol-like form) and C=O (1620 cm^{-1}, quinone-like form) suggests that OH^- could react with the thiophene ring of P($g_4$2T-TT). All the changes in the FTIR spectra agree with the degradation observed for polypyrrole and other polythiophenes.[31] To assess whether oxidized P($g_4$2T-TT) is susceptible to degradation by OH^-, we first doped the polymer in iron(III) chloride/acetonitrile solution and then immersed it in 0.1 M NaOH overnight (without voltage bias). As shown in Figure S13a (Supporting Information), the C=O signal increased when the polymer was positively charged, while no changes could be detected for the neutral polymer (Figure S13b, Supporting Information). The finding that OH^- is responsible for the degradation of p-type OMIECs during OECT operation agrees with the observation that even high-IE polymers, such as those based on DPP, which undergo four-electron ORR without H_2O_2 formation, experience degradation over prolonged periods.[9d]

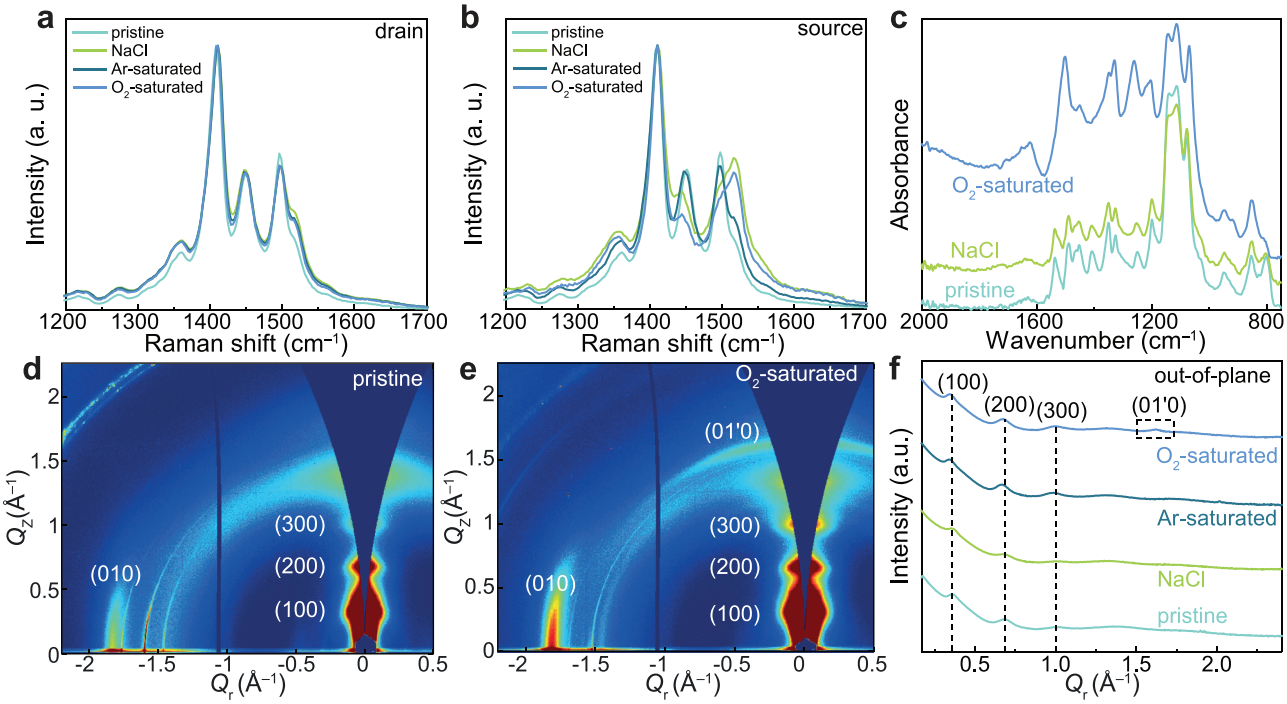

Figure 3. Raman spectra of P($g_4$2T-TT) near a) drain and b) source electrodes after devices pulsing cycling in Figure 1c. c) FTIR spectra of P($g_4$2T-TT) films after CV cycling. d,e) 2D GIWAXS pattern before and after CV cycling in O_2-saturated electrolyte. f) 1D out-of-plane line cuts of P($g_4$2T-TT) films after CV cycling.

Grazing incidence wide-angle X-ray scattering (GIWAXS) was used to study the crystalline structural changes occurring in P($g_4$2T-TT) during degradation (Figure 3d–f and Figure S14, Supporting Information). In agreement with previous reports,[29b,32] P($g_4$2T-TT) chains are mainly oriented edge-on with respect to the substrate. The (100) lamellar stacking peak shifts from 0.36 $Å^{-1}$ (d-spacing = 17.3 Å) to ≈0.34 $Å^{-1}$ (d-spacing = 18.3 Å) after cycling, as shown from the out-of-plane line cuts in Figure 3d. The lamellar spacing expansion indicates the ion intercalation into the side chains after electrochemical cycling.[29b,33] The (010) π–π stacking peak locates at ≈1.82 $Å^{-1}$ (d-spacing = 3.44 Å) and slightly shifts to lower q values by nearly 2% in the final fully undoped state (Figure 3f).[29b,33] Overall, the lattice structure does not change significantly, suggesting that degradation might affect the amorphous phase, which is known to be crucial for electronic conductivity.[11f,29a] However, a new face-on oriented π-stacking diffraction at $Q_z \approx 1.62$ $Å^{-1}$ (d-spacing = 3.88 Å) is shown after cycling in O_2-saturated NaCl, marked as (01'0) to distinguish it from the edge-on π–π stacking peak. The new (01'0) face-on diffraction peak may be attributed to disorder, as discussed for the FTIR and Raman spectra. Atomic force microscopy (AFM) measurements were carried out on top of drain, channel, and source areas before and after cycling in different electrolytes (Figure S15, Supporting Information). We observed negligible morphology changes in all areas regardless of the electrolyte.

Next, we developed an encapsulation strategy to suppress ORR and related OH^- formation that is at the origin of P($g_4$2T-TT) degradation, thus boosting the OECTs' stability. A polymer glue, comprising polyethylene oxide (PEO) and lithium bis(trifluoromethanesulfonyl)imide (LiTFSI), was coated on top of the channel area, following the procedure reported in the Experimental Section. The LiTFSI:PEO-based composite is used here as a protective layer to prevent ORR from happening at the channel's surface, thanks to its remarkable electrochemical stability and low water/oxygen permeability.[34] The weight fraction of LiTFSI (W_{LiTFSI}) was chosen to be 0.46 since, at this concentration, Li^+ coordinates with the PEO backbone's ether groups (Figures S16–S18, Supporting Information), yielding films that are insoluble in water.[35] In addition, the contribution of anions to the total ionic conductivity is maximal for $W_{LiTFSI} = 0.46$ (Figure S19, Supporting Information), which is preferable for p-type OECT operation.

Figure 4a illustrates the schematic of the OECT structure with the polymer glue layer placed between the P($g_4$2T-TT) channel and the 0.1 M NaCl aqueous electrolyte. Figure 4b and Figure S20 (in log scale, Supporting Information) show the P($g_4$2T-TT) OECT transfer characteristics with/without the polymer glue layer. Interestingly, the insertion of the LiTFSI:PEO layer does not affect the on/off ratio and max g_m values, while the hysteresis reduces compared to the OECTs without the polymer glue layer. We also observed a shift in V_{th} from −0.13 to 0 V upon insertion of the LiTFSI:PEO glue layer. This shift in V_{th} agrees with the shift in onset potential observed from CV (Figure S21, Supporting Information), and is attributed to the larger size of $TFSI^-$ anions compared to Cl^-[32] as also observed for P($g_4$2T-TT)-based OECTs measured using a 0.1 M LiTFSI solution as the electrolyte (Figure S22, Supporting Information).

We then investigated the operation stability of P($g_4$2T-TT)-based OECTs with/without the polymer glue layer. As shown in Figure 4c and Figure S23 (Supporting Information), OECTs

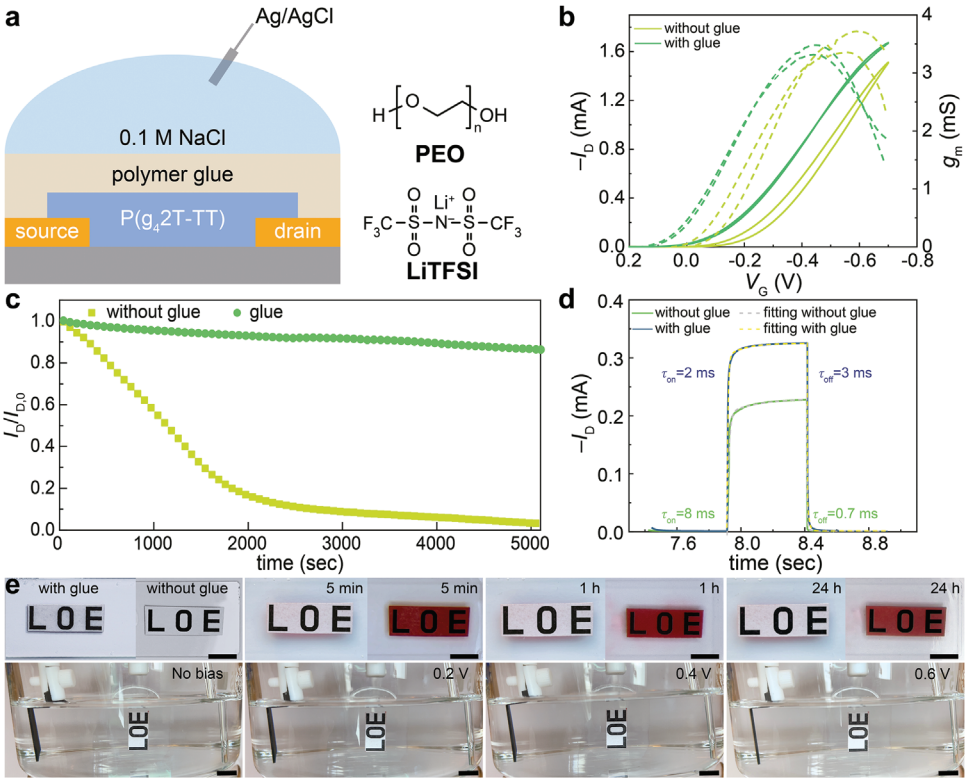

Figure 4. a) Cross-sectional schematic of OECT structure with the polymer glue layer. b) Transfer characteristics comparison (solid line) and corresponding transconductance (dash line) with/without glue layer. c) Long-term stability in pristine NaCl with/without glue (7 skip points). d) Temporal response and corresponding exponential fitting of the devices (W = 100 µm, L = 10 µm) with/without glue layer. e) Digital photos illustration of water resistance with polymer glue by immersing in NaCl and by applying different voltages for 10 min each. scale bar: 1 cm.

comprising the LiTFSI:PEO layer retain 85% of the initial current after nearly 2 h of continuous operation, a result which is comparable to that of P($g_4$2T-TT)-based OECTs in Ar-saturated electrolyte (see Figure 1c) and superior to what observed with the use of Lewis acids.[22] We argue that the observed improvement in stability with the LiTFSI:PEO layer is due to its low water uptake,[35] which suppresses ORR. The latter is confirmed by CV measurements, as reported in Figure S24 (Supporting Information). In the presence of O_2 and without the LiTFSI:PEO layer, a high polarized current is shown in the negative potential range, with the current increasing at higher O_2 content. In contrast, when the LiTFSI:PEO layer is used, the CV curves show a typical double-layer capacitance behavior in the negative potential range, suggesting that ORR is suppressed. This is equivalent to when Ar-saturated NaCl is used as the electrolyte. To confirm that water penetration is suppressed in the LiTFSI:PEO layer, we coated the latter on top of a water-sensitive label placed onto an FTO electrode (Figure 4e, see details in the Experimental Section). The water-sensitive label is such that it turns red in contact with water. The LiTFSI:PEO layer can prevent water from diffusing through it when immersed in 0.1 M NaCl for 24 h (without voltage bias) or when a voltage bias is applied for 10 min. In addition, oxygen diffusion is greatly reduced (Figure S25, Supporting Information). Note that we also tested the stability of P($g_4$2T-TT)-based OECTs, using 0.1 M LiTFSI as the electrolyte and in the absence of the LiTFSI:PEO layer, and observed a 70% drop in current after 450 cycles (Figure S26, Supporting Information). Therefore, the improved stability with the LiTFSI:PEO layer is not due to the LiTFSI salt. FTIR and Raman spectra show no sign of chemical degradation or microstructure changes when LiTFSI:PEO layer is coated on the channel layer (Figure S27, Supporting Information). For comparison, we tested the electrical performance of P($g_4$2T-TT)-OECTs comprising an ion exchange gel made of poly(vinylidene fluoride-*co*-hexafluoropropylene) (PVDF-HFP) and 1-ethyl-3-methylimidazolium bis(trifluoromethylsulfonyl)imide ([EMIM][TFSI]), similar to the one reported Bischak et al.,[36] but observed continuous degradation of the device performance (Figure S28, Supporting Information).

It is also interesting to note that the response time of P($g_4$2T-TT)-based OECTs with the LiTFSI:PEO glue layer is about four times faster (2 ms) compared to devices without the glue layer (8 ms, Figure 4d). We ascribed this to the higher ionic conductivity of the LiTFSI:PEO glue layer (Figure S29, Supporting Information). The ionic conductivity of 0.1 M NaCl is ≈6 mS cm^{-1}, but with the addition of the glue layer, it increases to 41 mS cm^{-1}. We attributed the significant enhancement in ionic conductivity observed for LiTFSI:PEO to the dissociation of LiTFSI salts in PEO, as discussed in Figures S16–18 (Supporting Information). Additionally, the diffusion of dehydrated chloride ions into the polymer glue layer (Figure S30, Supporting Information) could contribute to increasing the layer's anionic character. These two factors work together to reduce the charge transfer resistance at the electrode/electrolyte interfaces. The pristine glue layer has a

low ionic conductivity of ≈0.08 mS cm^{-1}, which leads to a large hysteresis in the OECT transfer curves when the glue is used as the sole electrolyte (Figure S31, Supporting Information).

3. Conclusions

In conclusion, we investigated the relationship between ORR and OECT degradation. By calibrating the electrochemical potential of each electrode, we determined that the ORR occurs on the surface of the drain electrode in p-type OECTs. We demonstrated that material degradation is caused by increased pH during ORR, which leads to the generation of excess OH^- on the drain electrode surface and penetration into the source electrode region when the OECT is switched on. This degradation by OH^- is irreversible and leads to instability in the device's performance. However, we also showed that using a polymer glue layer could improve the device's stability by preventing water and oxygen penetration. Devices with the protective polymer glue layer showed 85% current retention after ≈2 h of continuous doping/dedoping cycles in the saturation regime without compromising the switching speed and on/off ratio. This study could aid in the future design of stable and safe bioelectronic devices.

4. Experimental Section

Device Fabrications: All devices were fabricated on glass slides cleaned with sequential sonication in 2% Hellmanex, deionized water, acetone, and isopropanol. For larger devices (1000 × 30 µm), source and drain electrodes (5 nm Cr and 50 nm Au) were deposited by physical vapor deposition (PVD) using an evaporation mask (Source–Drain Deposition Mask for Low Density OFETs, Osilla Ltd, UK). For smaller devices (100 × 10 µm), the photolithography process was followed as reported.[17] P($g_4$2T-TT) was synthesized as reported.[23a] The film was deposited with 5 mg mL^{-1} chlorobenzene solution and spun at 1000 rpm for 60 s. For all the OECTs, an Ag/AgCl paste (Sigma–Aldrich) was used as the gate.

Electrical and Electrochemical Characterization: All the OECTs characteristics were tested by Keithley 4200 semiconductor parameter analyzer. The cyclic voltammetry and electrochemical impedance spectra were characterized by Bio-Logic Science Instruments. For all the cyclic voltammetry measurements, a three-electrode system was used with the P($g_4$2T-TT) electrode as the working electrode, a 2 cm^2 platinum mesh as the counter electrode, and an Ag/AgCl/saturated KCl (CHI Instrument) as the reference electrode. The CV samples obtained in NaCl electrolytes were cycled between −0.7 and 0.7 V, whereas in 0.1 M NaOH was cycled between −0.2 and 0.7 V versus Ag/AgCl/saturated KCl. P($g_4$2T-TT) electrode was spin-coated on 1 × 1 cm^2 Cr/Au electrode on a glass substrate. The ionic conductivity was measured by potentio-electrochemical impedance spectroscopy (PEIS) between 100 kHz and 100 mHz under open circuit potential conditions. The ionic conductivity of NaCl and NaCl+polymer glue was measured with a planar structure. For 0.1 M NaCl, a PDMS well with a 2 mm thick (d) and 2 mm wide (l) hole was covered on two parallel titanium electrodes with 3 mm distances (L). The NaCl+polymer glue sample was measured by covering 150-µm-thick glue on the same titanium electrodes with l = 9 mm. The ionic conductivity was calculated by $\sigma = \frac{L}{(l \times d) \times R}$[37] where R is the resistance obtained from the impedance at high frequency (Figure S22, Supporting Information). The polymer glue's ionic conductivity was measured by sandwiching 150-µm-thick polymer glue between two 3 × 9 mm^2 due to its low ionic conductivity.[38] The ionic conductivity was calculated by $\sigma = \frac{L}{A \times R}$ where A is the area of titanium electrodes.

Polymer Glue Preparation and Transformation: The polymer glue was prepared by dissolving 1.4 g PEO (Mw ≈600 000, Sigma–Aldrich) and 1.2 g LiTFSI (Sigma–Aldrich) in 10 mL acetone/dichloromethane binary solvent with 1:40 mass ratio.[34c,35] The uncrosslinked NFC film was prepared by mixing 50 g carboxymethylated nanofibrillated cellulose (1 wt.% solid content, ordered from Research Institutes of Sweden(RISE)), 25 mg glycerol (Sigma–Aldrich), and 50 g water by a laboratory mixer (T 10 basic ULTRA-TURRAX, IKA) for 30 min and then followed by degassing in a vacuum desiccator overnight to remove excessive bubbles in the viscous mixture. The NFC film was obtained by pouring the mixture in a Petri dish and dried at 60 °C for 3 h. The "double-sided tape" (see Figure S32, Supporting Information, for the illustration of the transfer process) was prepared by blade-coating the polymer glue on the NFC film in a liquid nitrogen slush bath to slow down the solvent evaporation. The polymer glue was transferred by directly sticking on the channel area of the devices. NFC film was peeled after spraying it with a small amount of water. Finally, devices were put into a vacuum oven at 60 °C overnight to remove the excess water and enhance the adhesion between the glue and the device.

H_2O_2 Detection: H_2O_2 was quantified by HRP-TMB (horseradish peroxidase-3,3',5,5'-tetramethylbenzidine) method. Ten microliters of each analyte were added to HRP-TMB buffer solution in a 96-well plate. The absorbance at 653 nm was then measured by a plate reader (BioTek Synergy H1 Hybrid Multi-Mode Microplate Reader). Finally, the concentration of produced H_2O_2 was determined by a calibration line, which was obtained from a known concentration of H_2O_2.

ORR Measurements: ORR measurements were performed on a BioLogic SP-200 Potentiostat with a typical three-electrode system. Ag/AgCl/saturated KCl and a platinum wire served as the reference and counter electrodes, respectively. Five microliters of P($g_4$2T-TT) in chlorobenzene solution (2.5 mg mL^{-1}) were drop-casted on a rotating disc electrode (RDE, area: 0.19625 cm^2, Pine Research Instrumentation) as the working electrode. The electrolyte (0.1 M NaCl) was purged with O_2 or Ar gas for at least 30 min before experiments, and the gas was kept for refreshing the headspace over the electrolyte during the experiments. The ORR activities were investigated by linear sweeping voltammetry (LSV) with a scan rate of 10 mV s^{-1} at different rotation speeds (400, 625, 900, 1225, 1600, 2025, and 2500 rpm) from 0.2 V to −0.8 V (vs Ag/AgCl/saturated KCl) under O_2 environment. The background current was acquired by LSV with a scan rate of 10 mV s^{-1} at 400 rpm from 0.2 V to –0.8 V (vs Ag/AgCl/saturated KCl) under an Ar atmosphere. The uncompensated resistance (R_u) was measured by potentiostatic electrochemical impedance spectroscopy (PEIS) between 100 kHz and 100 mHz under open circuit potential conditions. R_u was corrected after subtracting the background current. The electron transfer number (n) could be determined by the following Koutecký–Levich equation at different potentials:[25]

$$\frac{1}{J} = \frac{1}{J_K} + \frac{1}{J_{l,c}} = \frac{1}{J_K} + \frac{1}{0.201nFD^{2/3}\omega^{1/2}\nu^{-1/6}C_0} \quad (1)$$

where J, J_K, and $J_{l,c}$ are disk, kinetic, and diffusion-limited current density (mA cm^{-2}), respectively. F is the Faraday constant (96 485 C mol^{-1}), D is the diffusion coefficient of O_2 (1.9 × 10^{-5} cm^2 s^{-1}), ω is the angular speed in rpm, ν is the kinematic viscosity (0.01 cm^2 s^{-1}), and C_0 is the bulk concentration of O_2 (1.2 × 10^{-3} mol L^{-1}).

Materials Characterization: AFM was performed with a Dimension 3100 interfaced with a Nanoscope IV system operating in tapping mode. Silicon tips with a constant force of 40 N m^{-1} were used to record surface morphologies at room temperature and in ambient atmosphere. The samples for FTIR were measured after 100 CV cycles in a three-electrode system. The FTIR spectra (Bruker Equinox 55) were measured in ATR mode in ambient environment. The Raman spectra were measured with a Renishaw inVia Qontor confocal Raman microscope using a 50× long working distance objective. The excitation wavelength was 532 nm, and the Raman spectra were collected in the 150–2750 cm^{-1} range. Single measurements were measured with an excitation power of 0.1% or 1% with 2 s or 1 s accumulation time for OECT samples. The single measurements were repeated 90 times in a 15 by 6 grid with the measurement points separated by 5 µm, followed by cosmic ray and polynomial baseline removal from the single scans and averaging of the scans to achieve the final spectra. For GIWAXS measurement, the polymer was spin-coated onto Au-coated (80 nm)

silicon wafers at 1000 rpm for two layers. Samples were cycled between −0.7 and 0.7 V versus Ag/AgCl with a scan rate of 100 mV s^{-1} for 100 cycles. GIWAXS patterns were collected at a photon energy of 10.92 keV at an incident angle of $\theta = 0.14°$ at Argonne National Lab's (ANL's) Advanced Photon Source (APS) sector 8-ID-E. Scattering patterns were analyzed using GIXSGUI and custom MATLAB scripts.

Supporting Information

Supporting Information is available from the Wiley Online Library or from the author.

Acknowledgements

S.Z. thanks Jianfei Li for writing the program to extract the cycle stability data. The authors thank Xianjie Liu (Linköping University) for insightful discussions. This work was financially supported by the Knut and Alice Wallenberg Foundation (WWSC2.0), the Swedish Research Council (2020-03243), Olle Engkvists Stiftelse (204-0256), the European Commission through the FET-OPEN project MITICS (GA-964677), and the Swedish Government Strategic Research Area in Materials Science on Functional Materials at Linköping University (Faculty Grant SFO-Mat-LiU 2009-00971). T.-P.R. acknowledges support from the Academy of Finland (Postdoctoral Researcher No. 340103, Center of Excellence in Life-Inspired Hybrid Materials LIBER No. 346107, and the Flagship Programme on Photonics Research and Innovation PREIN No. 320165) and the European Union's Horizon 2020 research and innovation program under the Marie Skłodowska-Curie grant agreement No. 101022777. For the Raman spectra, this work used Tampere Microscopy Center facilities at Tampere University. R.W. and J.R. gratefully acknowledge support from the US National Science Foundation Grant No. NSF DMR-1751308. M.V. would like to acknowledge Swedish Research Council (VR 2019–05577, Flexible metal-air batteries).

Conflict of Interest

The authors declare no conflict of interest.

Data Availability Statement

The data that support the findings of this study are available from the corresponding author upon reasonable request.

Keywords

degradation, organic electrochemical transistors, p-type OECTs, stability

Received: February 26, 2023
Revised: May 19, 2023
Published online:

[1] a) D. Moia, A. Giovannitti, A. A. Szumska, I. P. Maria, E. Rezasoltani, M. Sachs, M. Schnurr, P. R. F. Barnes, I. McCulloch, J. Nelson, *Energy Environ. Sci.* **2019**, *12*, 1349; b) A. V. Volkov, H. Sun, R. Kroon, T.-P. Ruoko, C. Che, J. Edberg, C. Müller, S. Fabiano, X. Crispin, *ACS Appl. Energy Mater.* **2019**, *2*, 5350.

[2] a) Y. Jia, Q. Jiang, H. Sun, P. Liu, D. Hu, Y. Pei, W. Liu, X. Crispin, S. Fabiano, Y. Ma, *Adv. Mater.* **2021**, *33*, 2102990; b) M. Massetti, F. Jiao, A. J. Ferguson, D. Zhao, K. Wijeratne, A. Würger, J. L. Blackburn, X. Crispin, S. Fabiano, *Chem. Rev.* **2021**, *121*, 12465; c) Q. Jiang, H. Sun, D. Zhao, F. Zhang, D. Hu, F. Jiao, L. Qin, V. Linseis, S. Fabiano, X. Crispin, *Adv. Mater.* **2020**, *32*, 2002752; d) S. Wang, H. Sun, U. Ail, M. Vagin, P. O. Persson, J. W. Andreasen, W. Thiel, M. Berggren, X. Crispin, D. Fazzi, *Adv. Mater.* **2016**, *28*, 10764; e) A. Karki, A. J. Gillett, R. H. Friend, T.-Q. Nguyen, *Adv. Energy Mater.* **2021**, *11*, 2003441; f) D. Zhao, S. Fabiano, M. Berggren, X. Crispin, *Nat. Commun.* **2017**, *8*, 1; g) R. M. Pankow, J. Wu, A. Harbuzaru, B. Kerwin, Y. Chen, R. P. Ortiz, A. Facchetti, T. J. Marks, *Chem. Mater.* **2022**, *34*, 3267; h) A. C. Arango, L. R. Johnson, V. N. Bliznyuk, Z. Schlesinger, S. A. Carter, H.-H. Hörhold, *Adv. Mater.* **2000**, *12*, 1689; i) M. Skompska, *Synth. Met.* **2010**, *160*, 1; j) X. Zhou, F. Lv, Y. Huang, L. Liu, S. Wang, *Chem. - Eur. J.* **2020**, *26*, 15065; k) A. Malti, J. Edberg, H. Granberg, Z. U. Khan, J. W. Andreasen, X. Liu, D. Zhao, H. Zhang, Y. Yao, J. W. Brill, I. Engquist, M. Fahlman, L. Wågberg, X. Crispin, M. Berggren, *Adv. Sci.* **2016**, *3*, 1500305.

[3] a) M. Vagin, V. Gueskine, E. Mitraka, S. Wang, A. Singh, I. Zozoulenko, M. Berggren, S. Fabiano, X. Crispin, *Adv. Energy Mater.* **2021**, *11*, 2002664; b) M. Zhang, W. Yuan, B. Yao, C. Li, G. Shi, *ACS Appl. Mater. Interfaces* **2014**, *6*, 3587; c) R. P. Kingsborough, T. M. Swager, *Chem. Mater.* **2000**, *12*, 872; d) S.-N. Zhang, Z.-H. Xue, X. Lin, Y.-X. Lin, H. Su, S.-I. Hirano, X.-H. Li, J.-S. Chen, *J. Mater. Chem. A* **2020**, *8*, 19793.

[4] a) P. Andersson Ersman, R. Lassnig, J. Strandberg, D. Tu, V. Keshmiri, R. Forchheimer, S. Fabiano, G. Gustafsson, M. Berggren, *Nat. Commun.* **2019**, *10*, 5053; b) M. Berggren, X. Crispin, S. Fabiano, M. P. Jonsson, D. T. Simon, E. Stavrinidou, K. Tybrandt, I. Zozoulenko, *Adv. Mater.* **2019**, *31*, 1805813; c) S. Fabiano, N. Sani, J. Kawahara, L. Kergoat, J. Nissa, I. Engquist, X. Crispin, M. Berggren, *Sci. Adv.* **2017**, *3*, e1700345; d) P. A. Ersman, M. Zabihipour, D. Tu, R. Lassnig, J. Strandberg, J. Åhlin, M. Nilsson, D. Westerberg, G. Gustafsson, M. Berggren, *Flexible Printed Electron.*. **2020**, *5*, 024001.

[5] a) R. B. Rashid, X. Ji, J. Rivnay, *Biosens. Bioelectron.* **2021**, *190*, 113461; b) A. Nawaz, Q. Liu, W. L. Leong, K. E. Fairfull-Smith, P. Sonar, *Adv. Mater.* **2021**, *33*, 2101874; c) J. Chen, W. Huang, D. Zheng, Z. Xie, X. Zhuang, D. Zhao, Y. Chen, N. Su, H. Chen, R. M. Pankow, Z. Gao, J. Yu, X. Guo, Y. Cheng, J. Strzalka, X. Yu, T. J. Marks, A. Facchetti, *Nat. Mater.* **2022**, *21*, 564; d) H. Shim, F. Ershad, S. Patel, Y. Zhang, B. Wang, Z. Chen, T. J. Marks, A. Facchetti, C. Yu, *Nat. Electron.* **2022**, *5*, 660.

[6] a) P. Lin, F. Yan, J. Yu, H. L. W. Chan, M. Yang, *Adv. Mater.* **2010**, *22*, 3655; b) A. M. Pappa, D. Ohayon, A. Giovannitti, I. P. Maria, A. Savva, I. Uguz, J. Rivnay, I. McCulloch, R. M. Owens, S. Inal, *Sci. Adv.* **2018**, *4*, eaat0911; c) S. Wustoni, C. Combe, D. Ohayon, M. H. Akhtar, I. McCulloch, S. Inal, *Adv. Funct. Mater.* **2019**, *29*, 1904403; d) V. Druet, P. D. Nayak, A. Koklu, D. Ohayon, A. Hama, X. Chen, M. Moser, I. McCulloch, S. Inal, *Adv. Electron. Mater.*, *8*, 2200065.

[7] a) S. Park, S. W. Heo, W. Lee, D. Inoue, Z. Jiang, K. Yu, H. Jinno, D. Hashizume, M. Sekino, T. Yokota, K. Fukuda, K. Tajima, T. Someya, *Nature* **2018**, *561*, 516; b) P. Leleux, J. Rivnay, T. Lonjaret, J.-M. Badier, C. Bénar, T. Hervé, P. Chauvel, G. G. Malliaras, *Adv. Healthcare Mater.* **2015**, *4*, 142; c) M. Braendlein, T. Lonjaret, P. Leleux, J.-M. Badier, G. G. Malliaras, *Adv. Sci.* **2017**, *4*, 1600247; d) D. Khodagholy, T. Doublet, P. Quilichini, M. Gurfinkel, P. Leleux, A. Ghestem, E. Ismailova, T. Hervé, S. Sanaur, C. Bernard, G. G. Malliaras, *Nat. Commun.* **2013**, *4*, 1575; e) H. Lee, S. Lee, W. Lee, T. Yokota, K. Fukuda, T. Someya, *Adv. Funct. Mater.* **2019**, *29*, 1906982; f) X. Gu, S. Y. Yeung, A. Chadda, E. N. Y. Poon, K. R. Boheler, I.-M. Hsing, *Adv. Biosyst.* **2019**, *3*, 1800248; g) K. Lieberth, P. Romele, F. Torricelli, D. A. Koutsouras, M. Brückner, V. Mailänder, P. Gkoupidenis, P. W. M. Blom, *Adv. Healthcare Mater.* **2021**, *10*, 2100845.

[8] a) J. Y. Gerasimov, R. Gabrielsson, R. Forchheimer, E. Stavrinidou, D. T. Simon, M. Berggren, S. Fabiano, *Adv. Sci.* **2019**, *6*, 1801339; b) P.

Gkoupidenis, D. A. Koutsouras, G. G. Malliaras, *Nat. Commun.* **2017**, *8*, 15448; c) P. Gkoupidenis, N. Schaefer, B. Garlan, G. G. Malliaras, *Adv. Mater.* **2015**, *27*, 7176; d) S. Yamamoto, G. G. Malliaras, *ACS Appl. Electron. Mater.* **2020**, *2*, 2224; e) P. C. Harikesh, C.-Y. Yang, D. Tu, J. Y. Gerasimov, A. M. Dar, A. Armada-Moreira, M. Massetti, R. Kroon, D. Bliman, R. Olsson, E. Stavrinidou, M. Berggren, S. Fabiano, *Nat. Commun.* **2022**, *13*, 901; f) T. Nguyen-Dang, K. Harrison, A. Lill, A. Dixon, E. Lewis, J. Vollbrecht, T. Hachisu, S. Biswas, Y. Visell, T.-Q. Nguyen, *Adv. Electron. Mater.* **2021**, *7*, 2100519; g) G. Liu, Q. Li, W. Shi, Y. Liu, K. Liu, X. Yang, M. Shao, A. Guo, X. Huang, F. Zhang, Z. Zhao, Y. Guo, Y. Liu, *Adv. Funct. Mater.* **2022**, *32*, 2200959; h) G. Ciccone, M. Cucchi, Y. Gao, A. Kumar, L. M. Seifert, A. Weissbach, H. Tseng, H. Kleemann, F. Alibart, K. Leo, *DiscoverMater.* **2022**, *2*, 7; i) L. Petrauskas, M. Cucchi, C. Grüner, F. Ellinger, K. Leo, C. Matthus, H. Kleemann, *Adv. Electron. Mater.* **2022**, *8*, 2100330; j) M. Cucchi, C. Gruener, L. Petrauskas, P. Steiner, H. Tseng, A. Fischer, B. Penkovsky, C. Matthus, P. Birkholz, H. Kleemann, K. Leo, *Sci. Adv.* **2021**, *7*, eabh0693.

[9] a) M. Moser, A. Savva, K. Thorley, B. D. Paulsen, T. C. Hidalgo, D. Ohayon, H. Chen, A. Giovannitti, A. Marks, N. Gasparini, A. Wadsworth, J. Rivnay, S. Inal, I. McCulloch, *Angew Chem Int Ed Engl* **2021**, *60*, 7777; b) R. H. Karlsson, A. Herland, M. Hamedi, J. A. Wigenius, A. Åslund, X. Liu, M. Fahlman, O. Inganäs, P. Konradsson, *Chem. Mater.* **2009**, *21*, 1815; c) S. Inal, J. Rivnay, P. Leleux, M. Ferro, M. Ramuz, J. C. Brendel, M. M. Schmidt, M. Thelakkat, G. G. Malliaras, *Adv. Mater.* **2014**, *26*, 7450; d) A. Giovannitti, R. B. Rashid, Q. Thiburce, B. D. Paulsen, C. Cendra, K. Thorley, D. Moia, J. T. Mefford, D. Hanifi, D. Weiyuan, M. Moser, A. Salleo, J. Nelson, I. McCulloch, J. Rivnay, *Adv. Mater.* **2020**, *32*, 1908047; e) E. Zeglio, O. Inganäs, *Adv. Mater.* **2018**, *30*, 1800941; f) R. B. Rashid, A. M. Evans, L. A. Hall, R. R. Dasari, E. K. Roesner, S. R. Marder, D. M. D'Allesandro, W. R. Dichtel, J. Rivnay, *Adv. Mater.* **2022**, *34*, 2110703; g) T. Nguyen-Dang, S. Chae, J. Chatsirisupachai, H. Wakidi, V. Promarak, Y. Visell, T.-Q. Nguyen, *Adv. Mater.* **2022**, *34*, 2200274; h) X. Wu, T. L. D. Tam, S. Chen, T. Salim, X. Zhao, Z. Zhou, M. Lin, J. Xu, Y.-L. Loo, W. L. Leong, *Adv. Mater.* **2022**, *34*, 2206118.

[10] a) M. Hamedi, R. Forchheimer, O. Inganäs, *Nat. Mater.* **2007**, *6*, 357; b) M. Zabihipour, R. Lassnig, J. Strandberg, M. Berggren, S. Fabiano, I. Engquist, P. Andersson Ersman, *npj Flexible Electron.*. **2020**, *4*, 15; c) B. Schmatz, A. W. Lang, J. R. Reynolds, *Adv. Funct. Mater.* **2019**, *29*, 1905266; d) C. Qian, J. Sun, L.-a. Kong, G. Gou, J. Yang, J. He, Y. Gao, Q. Wan, *ACS Appl. Mater. Interfaces* **2016**, *8*, 26169; e) B. Marchiori, R. Delattre, S. Hannah, S. Blayac, M. Ramuz, *Sci. Rep.* **2018**, *8*, 8477; f) T. Nguyen-Dang, S. Chae, K. Harrison, L. C. Llanes, A. Yi, H. J. Kim, S. Biswas, Y. Visell, G. C. Bazan, T.-Q. Nguyen, *ACS Appl. Mater. Interfaces* **2022**, *14*, 12469.

[11] a) J. T. Friedlein, R. R. McLeod, J. Rivnay, *Org. Electron.* **2018**, *63*, 398; b) D. Tu, S. Fabiano, *Appl. Phys. Lett.* **2020**, *117*, 080501; c) D. A. Bernards, G. G. Malliaras, *Adv. Funct. Mater.* **2007**, *17*, 3538; d) L. Q. Flagg, R. Giridharagopal, J. Guo, D. S. Ginger, *Chem. Mater.* **2018**, *30*, 5380; e) B. D. Paulsen, S. Fabiano, J. Rivnay, *Annu. Rev. Mater. Res.* **2021**, *51*, 73; f) A. Savva, R. Hallani, C. Cendra, J. Surgailis, T. C. Hidalgo, S. Wustoni, R. Sheelamanthula, X. Chen, M. Kirkus, A. Giovannitti, *Adv. Funct. Mater.* **2020**, *30*, 1907657; g) S. E. Chen, L. Q. Flagg, J. W. Onorato, L. J. Richter, J. Guo, C. K. Luscombe, D. S. Ginger, *J. Mater. Chem. A* **2022**, *10*, 10738; h) L. Q. Flagg, C. G. Bischak, R. J. Quezada, J. W. Onorato, C. K. Luscombe, D. S. Ginger, *ACS Mater. Lett.* **2020**, *2*, 254; i) A. A. Szumska, I. P. Maria, L. Q. Flagg, A. Savva, J. Surgailis, B. D. Paulsen, D. Moia, X. Chen, S. Griggs, J. T. Mefford, R. B. Rashid, A. Marks, S. Inal, D. S. Ginger, A. Giovannitti, J. Nelson, *J. Am. Chem. Soc.* **2021**, *143*, 14795; j) R. Giridharagopal, J. Guo, J. Kong, D. S. Ginger, *ACS Appl. Mater. Interfaces* **2021**, *13*, 34616; k) L. Q. Flagg, C. G. Bischak, J. W. Onorato, R. B. Rashid, C. K. Luscombe, D. S. Ginger, *J. Am. Chem. Soc.* **2019**, *141*, 4345; l) M. Cucchi, A. Weissbach, L. M. Bongartz, R. Kantelberg, H. Tseng, H. Kleemann, K. Leo, *Nat. Commun.* **2022**, *13*, 4514.

[12] a) S. Zhang, M. Massetti, T.-P. Ruoko, D. Tu, C.-Y. Yang, X. Liu, Z. Wu, Y. Lee, R. Kroon, P. O. Å. Persson, H. Y. Woo, M. Berggren, C. Müller, M. Fahlman, S. Fabiano, *Adv. Funct. Mater.* **2022**, *32*, 2106447; b) S. Inal, G. G. Malliaras, J. Rivnay, *Nat. Commun.* **2017**, *8*, 1767.

[13] a) E. Mitraka, M. Gryszel, M. Vagin, M. J. Jafari, A. Singh, M. Warczak, M. Mitrakas, M. Berggren, T. Ederth, I. Zozoulenko, X. Crispin, E. D. Głowacki, *Adv. Sustainable Syst.* **2019**, *3*, 1800110; b) H. Peng, C. Soeller, N. Vigar, P. A. Kilmartin, M. B. Cannell, G. A. Bowmaker, R. P. Cooney, J. Travas-Sejdic, *Biosens. Bioelectron.* **2005**, *20*, 1821; c) W. Du, D. Ohayon, C. Combe, L. Mottier, I. P. Maria, R. S. Ashraf, H. Fiumelli, S. Inal, I. McCulloch, *Chem. Mater.* **2018**, *30*, 6164; d) A. Giovannitti, D.-T. Sbircea, S. Inal, C. B. Nielsen, E. Bandiello, D. A. Hanifi, M. Sessolo, G. G. Malliaras, I. McCulloch, J. Rivnay, *Proc Natl Acad Sci U S A.* **2016**, *113*, 12017.

[14] M. Moser, T. C. Hidalgo, J. Surgailis, J. Gladisch, S. Ghosh, R. Sheelamanthula, Q. Thiburce, A. Giovannitti, A. Salleo, N. Gasparini, A. Wadsworth, I. Zozoulenko, M. Berggren, E. Stavrinidou, S. Inal, I. McCulloch, *Adv. Mater.* **2020**, *32*, 2002748.

[15] a) I. P. Maria, B. D. Paulsen, A. Savva, D. Ohayon, R. Wu, R. Hallani, A. Basu, W. Du, T. D. Anthopoulos, S. Inal, J. Rivnay, I. McCulloch, A. Giovannitti, *Adv. Funct. Mater.* **2021**, *31*, 2008718; b) T. Nicolini, J. Surgailis, A. Savva, A. D. Scaccabarozzi, R. Nakar, D. Thuau, G. Wantz, L. J. Richter, O. Dautel, G. Hadziioannou, N. Stingelin, *Adv. Mater.* **2021**, *33*, 2005723; c) Y. Wang, E. Zeglio, H. Liao, J. Xu, F. Liu, Z. Li, I. P. Maria, D. Mawad, A. Herland, I. McCulloch, W. Yue, *Chem. Mater.* **2019**, *31*, 9797.

[16] M. Moser, L. R. Savagian, A. Savva, M. Matta, J. F. Ponder, Jr., T. C. Hidalgo, D. Ohayon, R. Hallani, M. Reisjalali, A. Troisi, A. Wadsworth, J. R. Reynolds, S. Inal, I. McCulloch, *Chem. Mater.* **2020**, *32*, 6618.

[17] E. A. Schafer, R. Wu, D. Meli, J. Tropp, M. Moser, I. McCulloch, B. D. Paulsen, J. Rivnay, *ACS Appl. Electron. Mater.* **2022**, *4*, 1391.

[18] N. A. Kukhta, A. Marks, C. K. Luscombe, *Chem. Rev.* **2022**, *122*, 4325.

[19] S. Dey, B. Mondal, S. Chatterjee, A. Rana, S. Amanullah, A. Dey, *Nat. Rev. Chem.* **2017**, *1*, 0098.

[20] a) E. Tan, J. Kim, K. Stewart, C. Pitsalidis, S. Kwon, N. Siemons, J. Kim, Y. Jiang, J. M. Frost, D. Pearce, J. E. Tyrrell, J. Nelson, R. M. Owens, Y.-H. Kim, J.-S. Kim, *Adv. Mater.* **2022**, *34*, 2202574; b) J. J. Samuel, A. Garudapalli, A. A. Mohapatra, C. Gangadharappa, S. Patil, N. P. B. Aetukuri, *Adv. Funct. Mater.* **2021**, *31*, 2102903.

[21] L. Kergoat, L. Herlogsson, B. Piro, M. C. Pham, G. Horowitz, X. Crispin, M. Berggren, *Proc Natl Acad Sci U S A.* **2012**, *109*, 8394.

[22] T. C. Hidalgo Castillo, M. Moser, C. Cendra, P. D. Nayak, A. Salleo, I. McCulloch, S. Inal, *Chem. Mater.* **2022**, *34*, 6723.

[23] a) D. Kiefer, R. Kroon, A. I. Hofmann, H. Sun, X. Liu, A. Giovannitti, D. Stegerer, A. Cano, J. Hynynen, L. Yu, Y. Zhang, D. Nai, T. F. Harrelson, M. Sommer, A. J. Moulé, M. Kemerink, S. R. Marder, I. McCulloch, M. Fahlman, S. Fabiano, C. Müller, *Nat. Mater.* **2019**, *18*, 149; b) K. Xu, H. Sun, T.-P. Ruoko, G. Wang, R. Kroon, N. B. Kolhe, Y. Puttisong, X. Liu, D. Fazzi, K. Shibata, C.-Y. Yang, N. Sun, G. Persson, A. B. Yankovich, E. Olsson, H. Yoshida, W. M. Chen, M. Fahlman, M. Kemerink, S. A. Jenekhe, C. Müller, M. Berggren, S. Fabiano, *Nat. Mater.* **2020**, *19*, 738.

[24] D. Li, B. Wang, X. Long, W. Xu, Y. Xia, D. Yang, X. Yao, *Angew. Chem., Int. Ed.* **2021**, *60*, 26483.

[25] J. Zhang, Z. Xia, L. Dai, *Sci. Adv.* **2015**, *1*, e1500564.

[26] G. Fu, S. T. Sanjay, W. Zhou, R. A. Brekken, R. A. Kirken, X. Li, *Anal. Chem.* **2018**, *90*, 5930.

[27] B.-T. Zhang, L.-X. Zhao, J.-M. Lin, *J. Environ. Sci.* **2008**, *20*, 1006.

[28] T. Kwon, Y. Lim, J. Cho, R. Lawler, B. J. Min, W. A. Goddard, S. S. Jang, J. Y. Kim, *Mater. Today* **2022**, *58*, 135.

[29] a) A. Savva, C. Cendra, A. Giugni, B. Torre, J. Surgailis, D. Ohayon, A. Giovannitti, I. McCulloch, E. Di Fabrizio, A. Salleo, J. Rivnay, S. Inal,

Chem. Mater. **2019**, *31*, 927; b) B. D. Paulsen, A. Giovannitti, R. Wu, J. Strzalka, Q. Zhang, J. Rivnay, C. J. Takacs, *Small* **2021**, *17*, 2103213; c) J. Gao, A. K. Thomas, R. Johnson, H. Guo, J. K. Grey, *Chem. Mater.* **2014**, *26*, 4395; d) T. J. Quill, G. LeCroy, A. Melianas, D. Rawlings, Q. Thiburce, R. Sheelamanthula, C. Cheng, Y. Tuchman, S. T. Keene, I. McCulloch, R. A. Segalman, M. L. Chabinyc, A. Salleo, *Adv. Funct. Mater.* **2021**, *31*, 2104301.

[30] J. Razzell-Hollis, F. Fleischli, A. A. Jahnke, N. Stingelin, D. S. Seferos, J.-S. Kim, *J. Phys. Chem. C* **2017**, *121*, 2088.

[31] a) G. Zotti, G. Schiavon, S. Zecchin, *Synth. Met.* **1995**, *72*, 275; b) Y. Li, R. Qian, *Electrochim. Acta* **2000**, *45*, 1727; c) Y. Li, R. Qian, *Synth. Met.* **1993**, *53*, 149.

[32] C. Cendra, A. Giovannitti, A. Savva, V. Venkatraman, I. McCulloch, A. Salleo, S. Inal, J. Rivnay, *Adv. Funct. Mater.* **2019**, *29*, 1807034.

[33] J. O. Guardado, A. Salleo, *Adv. Funct. Mater.* **2017**, *27*, 1701791.

[34] a) H. Wang, J. K. Keum, A. Hiltner, E. Baer, *Macromolecules* **2009**, *42*, 7055; b) H. Chen, D. Adekoya, L. Hencz, J. Ma, S. Chen, C. Yan, H. Zhao, G. Cui, S. Zhang, *Adv. Energy Mater.* **2020**, *10*, 2000049; c) M. Echeverri, N. Kim, T. Kyu, *Macromolecules* **2012**, *45*, 6068; d) H. Lin, B. D. Freeman, *J. Membr. Sci.* **2004**, *239*, 105.

[35] Y. Jiao, F. Li, X. Jin, Q. Lei, L. Li, L. Wang, T. Ye, E. He, J. Wang, H. Chen, J. Lu, R. Gao, Q. Li, C. Jiang, J. Li, G. He, M. Liao, H. Zhang, I. P. Parkin, H. Peng, Y. Zhang, *Adv. Funct. Mater.* **2021**, *31*, 2107652.

[36] C. G. Bischak, L. Q. Flagg, D. S. Ginger, *Adv. Mater.* **2020**, *32*, 2002610.

[37] Y. Hu, V. Miikkulainen, K. Mizohata, T. Norby, O. Nilsen, H. Fjellvåg, *Electrochim. Acta* **2020**, *361*, 137019.

[38] S. Zhang, N. Yu, S. Zeng, S. Zhou, M. Chen, J. Di, Q. Li, *J. Mater. Chem. A* **2018**, *6*, 12237.